14

Issues on Interfacing Problematics in PV Generator and MPP-Tracking Converters

Teuvo Suntio
Tampere University of Technology,
Department of Electrical Energy Engineering
Finland

1. Introduction

The need for large-scale harvesting of renewable and clean energy such as solar or photovoltaic (PV) energy has been recently fully recognized for reducing greenhouse gas emissions and securing the availability of energy in the future (Bull, 2001; Bose, 2010; Rahman, 2008). PV energy can be utilized by converting it into thermal energy or directly to electrical energy by means of solar cells (Rahman, 2008).

The simplified electrical equivalent model of a solar cell composes of a photocurrent source and a diode connected across the current source as depicted in Fig. 1a (Lyi & Dougal, 2002; Villalva, et al., 2009). The solar cell is a highly non-linear and non-ideal current source yielding limited output voltage and power as depicted in Fig. 1b. In addition with the non-linear static terminal behaviour, its dynamic behaviour in terms of dynamic resistance and capacitance is equally non-linear and dependent on the operating point (Anantha Krishna, et al., 2011; Kumar, et al., 2006; Mäki, et al., 2010; Thongpron, et al., 2006). Typical maximum voltage of a single-junction silicon cell is in the order of 0.5 V (Kumar, et al., 2006). As a consequence, a large number of cells usually have to be connected in series to form a PV generator for fulfilling the practical solar energy harvesting.

In order to maximally utilize the energy provided by the PV generator, its operating point has to be kept at the maximum power point (MPP) (Fig. 1b, the point (1,1)), where the static and dynamic resistances coincide (Thongpron, et al., 2006; Xiao, et al., 2007a) according to the maximum power theorem (MacLaughlin & Kaiser, 2007). Innumerable methods and algorithms have been developed for tracing the location of the MPP as discussed e.g. in (Esram & Chapman, 2007; Jain & Agarwal, 2007; Salas, et al., 2006).

The output of a PV generator is very seldom suited as such for powering the load because of its highly varying terminal characteristics due to the changes in the environmental conditions such as ambient temperature, level of irradiation, cloud passing, etc. The terminal characteristics in Fig. 1b imply that the PV generator exhibits both constant-current-source behaviour and constant-voltage-source behaviour as well. The dynamic characteristics (i.e., the dynamic resistance (r_{sc})) in Fig. 1b confirm also the dual source nature. In practice, this means that the interfacing can be accomplished either by using voltage-fed (VF) or current-fed (CF) converters (Capel, et al., 1983) but the different

interfacing constraints such as the validity of Kirchhoff's current law and stability under output-side feedback control have to be carefully considered (Suntio, et al., 2010a&b).

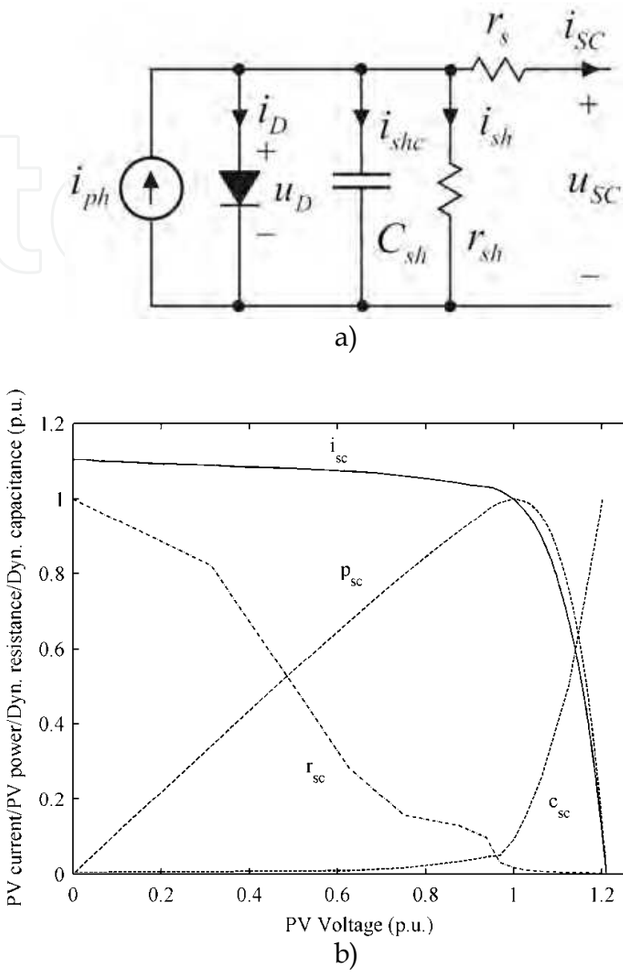

Fig. 1. Solar cell characteristics: a) Simplified electrical model, and b) static and dynamic terminal characteristics as normalized I/U, P/U, r/U, and c/U curves

In order to supply maximum power from the energy source, the feedback-control arrangement shall be such that the input-side feedback loop is the outmost loop within every converter in the process as depicted in Fig. 2. The dual source nature of the PV generator makes it possible to use either conventional VF converters or CF converters as the interfacing media. According to control engineering principles (Suntio, 2009), the input current of a VF converter and the input voltage of a CF converter have to be used as the feedback variables. This means, in practice, that the feedback arrangements determine also the nature and dynamic behaviour of the converter. Despite this fact, it is usual that the distinction between the VF and CF interfacing converters is not made but all the converters are considered to be conventional VF converters as in (Dehbonei, et al., 2009a&b; Femia, et al., 2008) even if special control arrangements (i.e., inversing the polarity of the feedback and reference signals in the controller) have to be made for proper operation as explicitly shown e.g. in (Siri, 2001). The same applies also to the grid-connected inverters in the renewable

energy applications as depicted in Fig. 2. The lack of real recognition of the static and dynamic differences in the converters compared to the conventional converters has led to a situation, where the proposed PV converters have not been tested by using a proper input source as discussed e.g. in (Menti, et al., 2011; Sanchis, et al., 2007). Therefore, the suitability of the converter for the intended application has to be carefully tested by using a real PV generator or a solar array simulator, which is known to have the same static and dynamic properties as the real PV generator.

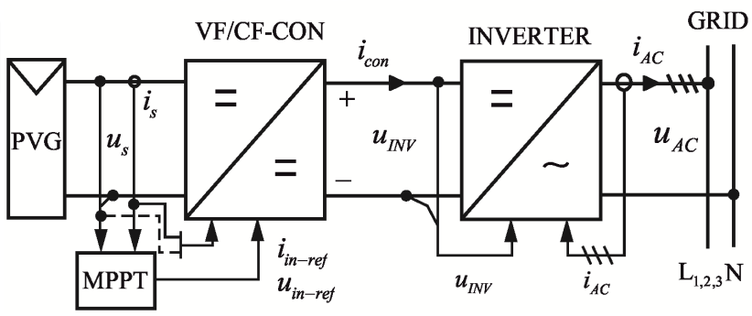

Fig. 2. Principle of grid-connected PV energy system in grid-parallel operation mode

According to (Petrone, et al., 2008), there are a number of issues related to the MPP-tracking converters and grid-connected inverters, which reduce the reliability of the PV energy systems. One of those issues is the stability of the interconnected system, which can be assessed at an arbitrary interface within the system by means of the small-signal impedances determined for the upstream (source) and downstream (load) subsystems at the selected interface (Middlebrook, 1976; Suntio, et al., 2010a&b; Zenger, et al., 2006).

The rest of the chapter will treat the topics discussed above more in detail and is organized as follows: The basic static and dynamic properties of a real PV panel are introduced in Section 2 including the effect of partial shading (Wang&Hsu, 2011) as well as the characterization of a certain commercial solar array simulator as a substitute for the real PV generator. General dynamic representations of interfacing converters are given in Section 3 including the parameters affecting mostly the quality of the interfacing as well as stability of the system. A short introduction to the implementation CF converters is given in Section 4. Experimental evidence is provided in Section 5 to validate the theoretical findings presented in Section 3. Section 6 summarizes the topics of the chapter and recommends further actions to be taken.

2. Basic properties of a PV generator

The current-voltage characteristics of a PV cell can be represented with sufficient accuracy by using the single-diode equation given in (1) (Lyi & Dougal, 2002), where i_{sc} and u_{sc} are the current and voltage of the cell, i_{ph} is the light-generated current, i_0 the diode saturation current, r_s the series resistance, r_{sh} the shunt resistance, A the diode ideality factor, k the Boltzmann constant, T the cell temperature, and q the elementary charge. The PV generator consists of series-connected cells. As a consequence, its current-voltage characteristics can be given by adding the effect of the number of series-connected cells N_s in the single-diode equation as shown in (1). Naturally, $N_s = 1$ for a single cell.

$$i = i_{ph} - i_0 \left[\exp\left(\frac{u_{sc} + r_s i_{sc}}{N_s AkT / q} \right) - 1 \right] - \frac{u_{sc} + r_s i_{sc}}{r_{sh}} \quad (1)$$

The electrical equivalent circuit corresponding to (1) is given in Fig. 1a. The behaviour of the dynamic resistance (r) and capacitance (c) of the PV module (See Fig. 1) can be easily understood based on the behaviour of a silicon diode and constant-current source: If the diode current is low, the resistance of the circuit is high and capacitance low. The increase in the diode current reduces the resistance and increases the capacitance. The circuit exhibits lowest resistance and highest capacitance at the open-circuit condition, because all the photocurrent is flowing through the diode.

The silicon diode has a negative temperature coefficient approximately of -2.5 mV/^{o}C (Anantha Krishna, et al., 2011). This means that the voltage and maximum output power of the PV generator decreases along the increase in the cell temperature and vice versa but the photocurrent remains effectively constant. The effect of the temperature on the resistance and capacitance is such that the resistance decreases and capacitance increases along the increase in the temperature and naturally vice versa.

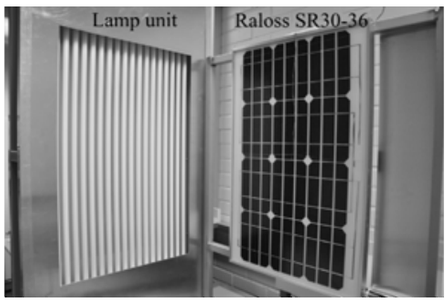

Fig. 3. Fluorescent lamp unit and Raloss SR30-36 PV module

The above described behaviour of the dynamic parameters without the temperature effect is clearly visible in Fig. 1b, where all the curves represent normalized measured data from an actual PV module of Raloss SR30-36, which is illuminated by using a lamp unit shown in Fig. 3 producing illumination of 500 W/m^2. The corresponding short-circuit current and open-circuit voltage are 1.0 A and 19.2 V as well as the MPP current and voltage 0.91 A and 16.0 V at the module temperature of 44 ^{o}C, respectively.

The experimental frequency responses shown below are extracted from the PV module by means of Venable Industries' frequency response analyzer Model 3120 with an impedance measurement kit. The dynamic resistance is extracted from the measurements at the frequency of 100 Hz. The dynamic capacitance is extracted based on the cut-off frequency of the first-order filter behaviour or the resonant frequency caused by the cabling inductance of 2 μH and the capacitance of the generator.

2.1 Dynamic resistance and capacitance

The measured output impedances of Raloss SR30-36 panel from the short-circuit (SC) to open-circuit (OC) conditions are shown in Fig. 4. The low-frequency dynamic resistance is explicitly normal positive resistance not negative resistance as assumed e.g. by (Xiao, et al.,

2007a). It is extremely important that the behaviour of the low-frequency dynamic resistance is correctly considered when analyzing its effect on the dynamic behaviour of the interfacing converters, otherwise the result of the dynamic analyses are incorrect as e.g. in (Xiao, et al., 2007a&b; Femia, et al., 2008). The measured dynamic resistance at the dark current conditions as in (Xiao, et al., 2007a) does not correctly match with the real dynamic resistance experienced at the illuminated or normal conditions as clearly shown in (Mäki, et. al., 2010).

The extracted operating-point-dependent dynamic resistance and capacitance values are shown in Fig. 5, where the normalizing factors are 1 kΩ and 22 µF, respectively. Fig. 6 shows the behaviour of the static ($r_{con} = U_{pv}/I_{pv}$) and dynamic resistance (r_{sg}) of the PV panel in the vicinity of the MPP: The resistances coincide at the MPP.

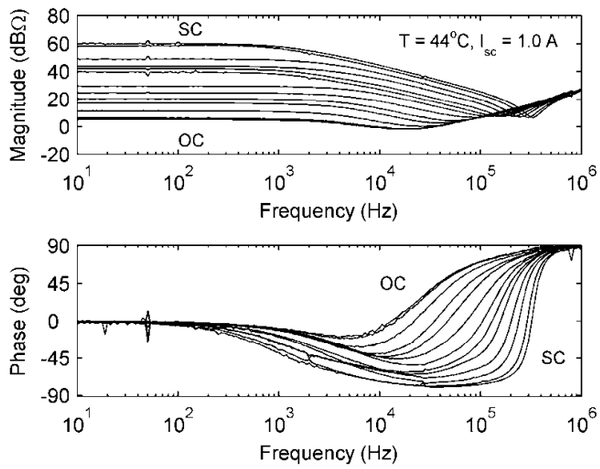

Fig. 4. The measured output impedances of Raloss SR30-36 panel from the short-circuit (SC) to open-circuit (OC) conditions

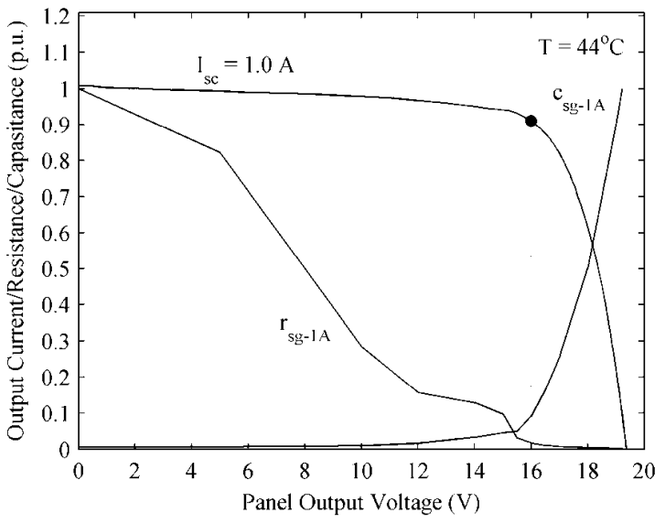

Fig. 5. The measured dynamic resistance and capacitance, where the scaling factors are 1 kΩ and 22 µF

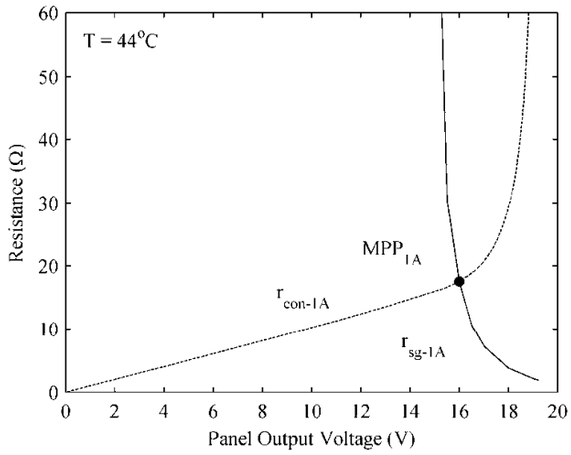

Fig. 6. The behaviour of the static ($r_{con\text{-}1A}$) and dynamic ($r_{sg\text{-}1A}$) resistances in the vicinity of MPP

2.2 Shading effect

Two Raloss SR30-36 panels were connected in series and Schotky-type shunt diodes were connected across each panel. One of the panels was illuminated as defined above and the other with reduced illumination yielding short-circuit current of 0.3 A, respectively. Fig. 7 shows the measured IU curves for the individual panels ($I_{sg\text{-}1}$, $I_{sg\text{-}2}$) and the series connection ($I_{sg\text{-}tot}$)) of them. The behaviour of the dynamic resistance is shown in Fig. 8, respectively.

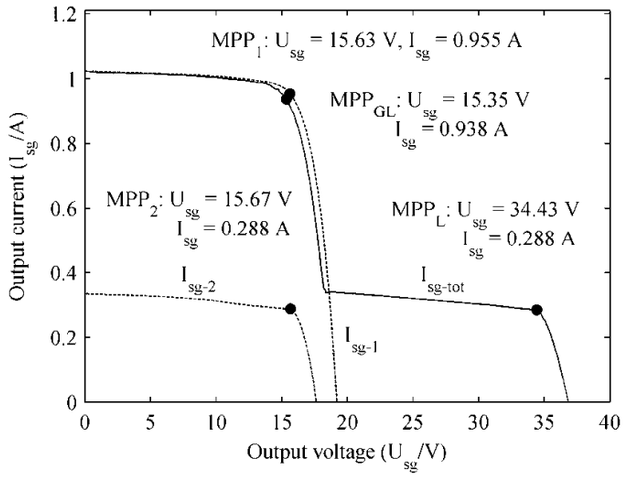

Fig. 7. The static IU curves of the individual panels and their series connection

The static and dynamic resistances will coincide at each of the MPPs. Fig. 8 implies also clearly that each of the MPPs divides the operation of the PV generator into constant-current and constant-voltage sub-regions, which will limit the operation of the VF converters in the constant-voltage region at the voltages higher than the highest-voltage MPP. The behaviour of the dynamic resistance implies also problems for the performance of the incremental-conductance-based methods to locate the real global MPP.

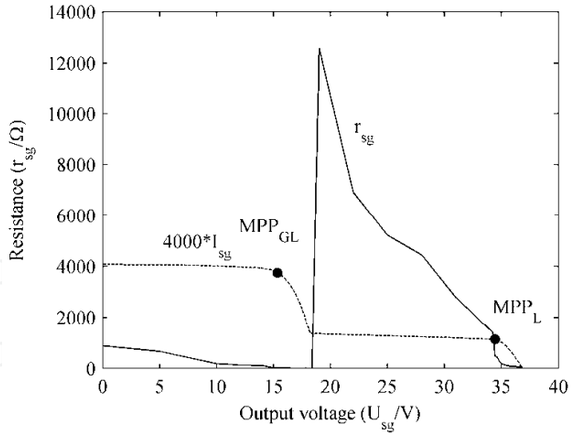

Fig. 8. The behaviour of the dynamic resistance r_{sg} of the series connected panels

2.3 Solar array simulator

It is not very well understood that the PV generator has unique properties resembling both constant-current and constant-voltage sources. As a consequence of this, the PV generator is most often considered to be just a voltage source with rather high output impedance especially when a capacitor is always connected between the PV generator and the interfacing converter. Therefore, the proposed converters may not be tested at all by using a real PV generator or a source simulator having the dynamic properties similar to the real PV generator (Menti, et al., 2011; Sanchis, et al., 2007). Usually a pure constant-voltage source with a small resistance in series is only used as in (Park, et al., 2006). As discussed above, it is, however, extremely important that the input source has the characteristics of a PV generator especially in respect to the dynamic-impedance behaviour.

A certain commercial solar array simulator (SAS) was programmed to emulate the behaviour of the Raloss SR30-36 panel by using the voltage and current of the three remarkable points (OC, SC, and MPP) (Villalva, et al., 2009). The resulting static IU curves are presented in Fig. 9 showing a perfect match in the constant-current region but a slight deviation in the constant voltage region.

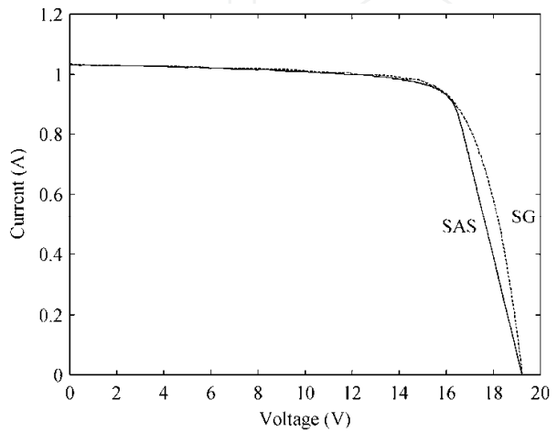

Fig. 9. The measured static IU curves of the Raloss panel (SG) and the solar array simulator (SAS)

The frequency responses of the solar array simulator were measured and the dynamic resistance was extracted similarly to the Raloss panel. The comparison of the dynamic resistances is shown in Fig. 10, where Fig. 10a shows the overall behaviour of resistances, and Fig. 10b, the behaviour of resistances in the vicinity of the MPP. The overall dynamic resistance of the SAS emulates quite well the dynamic resistance of the Raloss panel. It can be expected that the testing with such an input source would very well ensure the working of the tested converters also in the practical applications. The reason for the inaccuracy of the static curve in the constant-voltage region is the method to establish the output resistance as a constant value of approximately three ohms as shown in Fig. 10b.

A multitude of proposed techniques to design solar array simulators can be found in the open literature but they are very seldom characterized in such way that their dynamic properties are shown. The correct dynamic behaviour of the electronic solar array simulator may be possible only when the base of the simulator is a real current source.

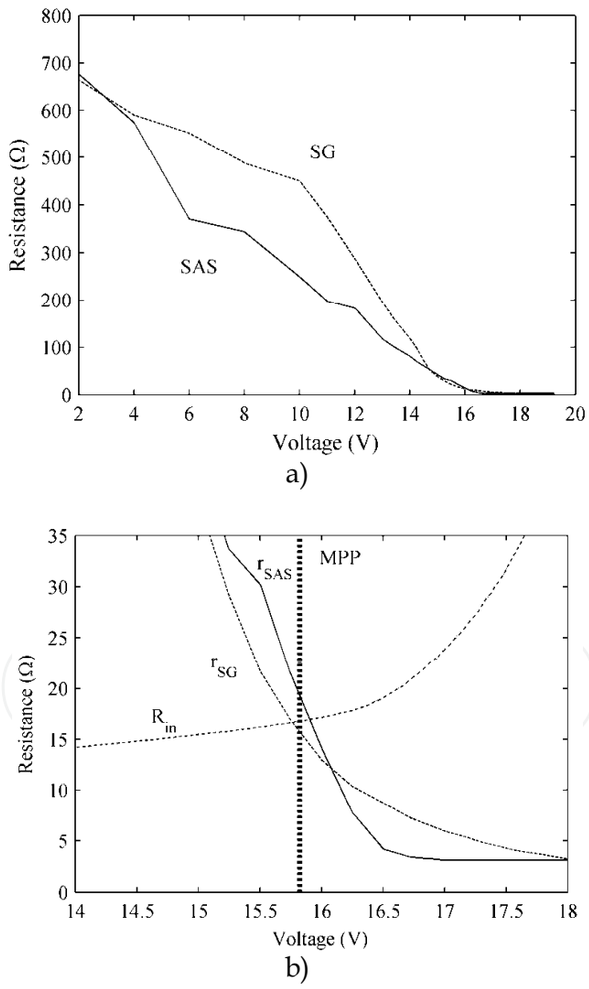

Fig. 10. The comparison of dynamic resistances of the Raloss panel (r_{SG}) and a commercial solar array simulator (r_{SAS}): a) Overall impedance behaviour, and b) behaviour in the vicinity of the MPP, where R_{in} is the static resistance of the PV generator and the simulator

3. General dynamic representations

The dynamics of a switched-mode converter can be represented by using certain two-port-network parameters, which are uniquely determined by the input and output sources as well as the output variable kept constant (Suntio, 2009). It shall be noted that a resistor as a load does not change the output mode of a converter but the load has to be either a constant-current or constant-voltage-type source. In general, the converters can be classified as voltage and current-fed converters based on their actual input source. Their output mode can be further classified into voltage and current. As a consequence, there exist four different types of converters- namely voltage-to-voltage, voltage-to-current, current-to-current, and current-to-voltage converters, which can be represented by means of G, Y, H, and Z network parameters, respectively (Tse, 1998). The corresponding two-port models are shown in Fig. 11. The output mode in Fig. 11 is visible as the dual of the ideal load. It shall be also noted that the direction of the output current is opposite what is used in the theoretical two-port-network models (Tse, 1998).

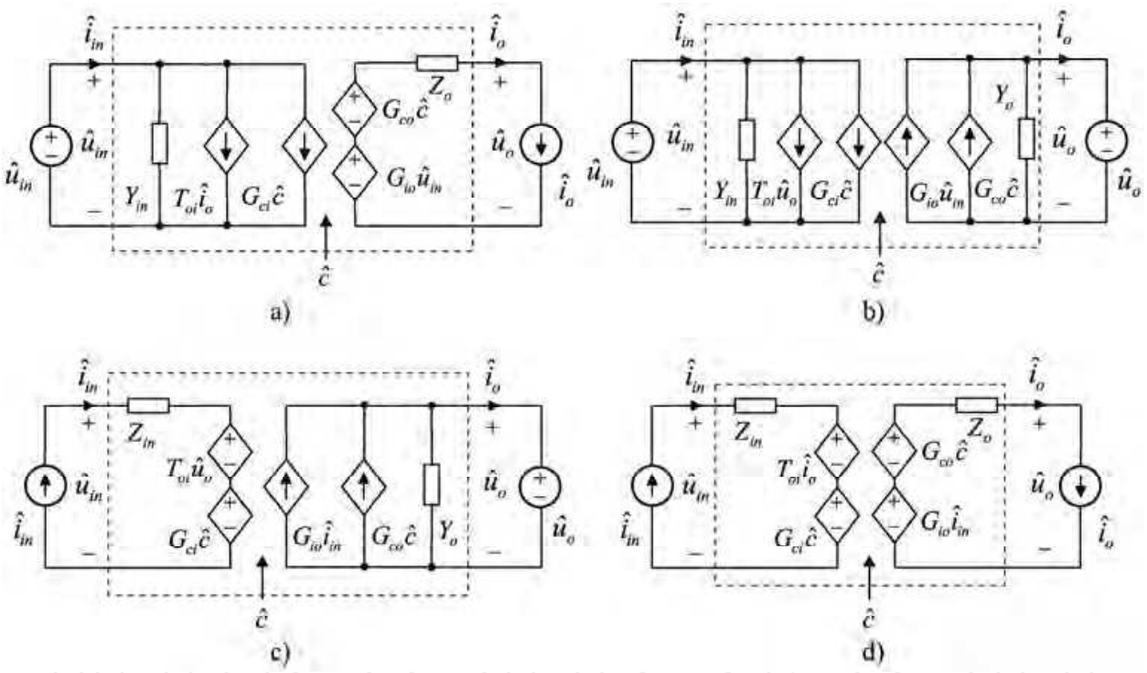

Fig. 11. Linear two-port models representing converters defined by a) G, b) Y, c) H, and d) Z parameters

According to Fig. 11, it may be obvious that only the current-fed converters (Figs. 11c&d) can offer an ideal interfacing condition for the PV generator due to its current-source nature at the input terminal, because the ideal interfacing requires the existence of duality in the connection interface (Suntio, et al., 2010b). The voltage-fed converters (Fig. 11a&b) are prone to the violation of Kirchhoff's current law when the operating point moves into the voltages below the MPP (Suntio, et al., 2010a). The nature of the input port shown in Fig. 11 is valid also at steady state justifying the above presented conclusions.

3.1 General treatment of the converter dynamics

The two-port models shown in Fig. 11 can be equally represented by using matrix representations having typically three input variables $\left[\hat{x}_{\text{in}} \quad \hat{x}_{\text{out}} \quad \hat{x}_{\text{c}}\right]^T$ and two output variables $\left[\hat{y}_{\text{in}} \quad \hat{y}_{\text{out}}\right]^T$, where the subscript 'in' denotes the variables at the input terminal, 'out' the variables at the output terminal, and 'c' the general control variable. The variables can be either voltage or current. This yields six transfer functions G_{ij} shown in (2). The sign of the transfer function G_{22} is minus, because the direction of current at the output terminal is opposite (See Fig. 11) what is generally defined for the two-port networks as shown in (Tse, 1998).

$$\begin{bmatrix} \hat{y}_{\text{in}} \\ \hat{y}_{\text{out}} \end{bmatrix} = \begin{bmatrix} G_{11} & G_{12} & G_{13} \\ G_{21} & -G_{22} & G_{23} \end{bmatrix} \begin{bmatrix} \hat{x}_{\text{in}} \\ \hat{x}_{\text{out}} \\ \hat{x}_{\text{c}} \end{bmatrix} \tag{2}$$

3.1.1 Converter under feedback control

According to the control engineering principles (Suntio, 2009), the feedback can be based only on the output variables of the system (i.e., $\hat{y}_{\text{in}}$ and $\hat{y}_{\text{out}}$) yielding two different sets of closed-loop transfer functions. Under the input-side feedback control, the closed-loop transfer functions can be presented as shown in (3) based on Fig. 12, where the subscript 'o' denotes the open-loop transfer functions, $L_{\text{in}} = G_{\text{se-in}}G_{\text{a}}G_{\text{c-in}}G_{13}$ the input-side loop gain, $G_{\text{se-in}}$ the input-side sensor gain, G_{a} the modulator gain, and $G_{\text{c-in}}$ input-side-controller transfer function, respectively. Input variable $\hat{x}_{\text{r-in}}$ is the reference for the controlled variable. The special transfer functions $G_{21-\infty}$ and $G_{22-\infty}$ are known as certain ideal output-side transfer functions and defined in (4).

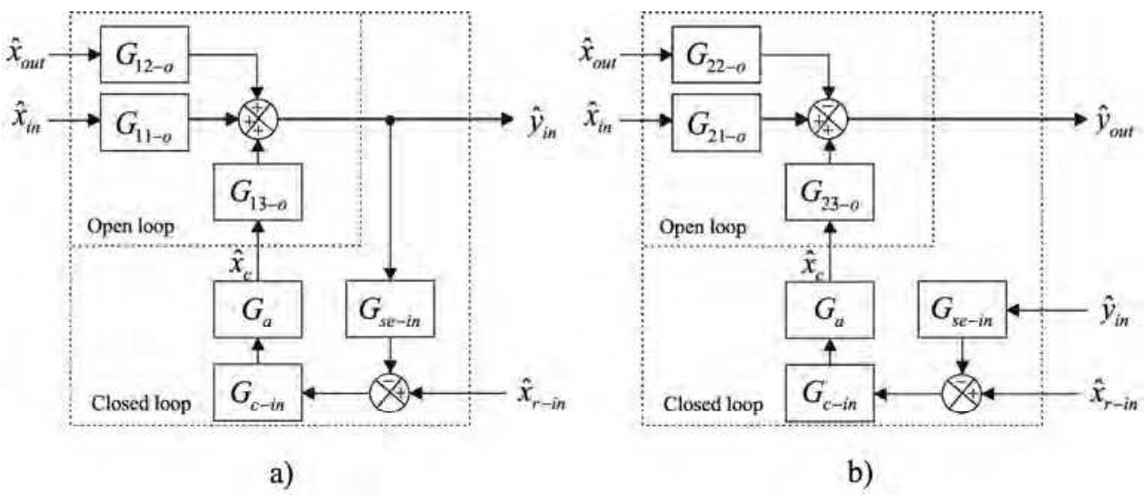

Fig. 12. General closed-loop a) input and b) output control block diagrams under input-side control

$$\begin{bmatrix}\hat{y}_{\text{in}}\\ \hat{y}_{\text{out}}\end{bmatrix}=\begin{bmatrix}\dfrac{G_{11\text{-o}}}{1+L_{\text{in}}} & \dfrac{G_{12\text{-o}}}{1+L_{\text{in}}} & \dfrac{1}{G_{\text{se-in}}}\dfrac{L_{\text{in}}}{1+L_{\text{in}}}\\ \left(\dfrac{G_{21\text{-o}}}{1+L_{\text{in}}}+\dfrac{L_{\text{in}}G_{21\text{-}\infty}}{1+L_{\text{in}}}\right) & -\left(\dfrac{G_{22\text{-o}}}{1+L_{\text{in}}}+\dfrac{L_{\text{in}}G_{22\text{-}\infty}}{1+L_{\text{in}}}\right) & \dfrac{G_{23\text{-o}}}{G_{\text{se-in}}E_{13\text{-o}}}\dfrac{L_{\text{in}}}{1+L_{\text{in}}}\end{bmatrix}\begin{bmatrix}\hat{x}_{\text{in}}\\ \hat{x}_{\text{out}}\\ \hat{x}_{\text{r-in}}\end{bmatrix} \tag{3}$$

$$G_{21\text{-}\infty}=G_{21\text{-o}}-\frac{G_{11\text{-o}}G_{23\text{-o}}}{G_{13\text{-o}}}\qquad G_{22\text{-}\infty}=G_{22\text{-o}}+\frac{G_{12\text{-o}}G_{23\text{-o}}}{G_{13\text{-o}}} \tag{4}$$

Under the output-side control, the closed-loop transfer functions can be presented as shown in (5) based on Fig. 13, where the subscript 'o' denotes open-loop transfer functions, $L_{\text{out}}=G_{\text{se-out}}G_{\text{a}}G_{\text{c-out}}G_{23}$ the output-side loop gain, $G_{\text{se-out}}$ the output-side sensor gain, G_{a} the modulator gain, and $G_{\text{c-out}}$ output-side-controller transfer function, respectively. Input variable $\hat{x}_{\text{r-out}}$ is the reference for the controlled variable. The special transfer functions $G_{11-\infty}$ and $G_{12-\infty}$ are known as certain ideal input-side transfer functions and defined in (6).

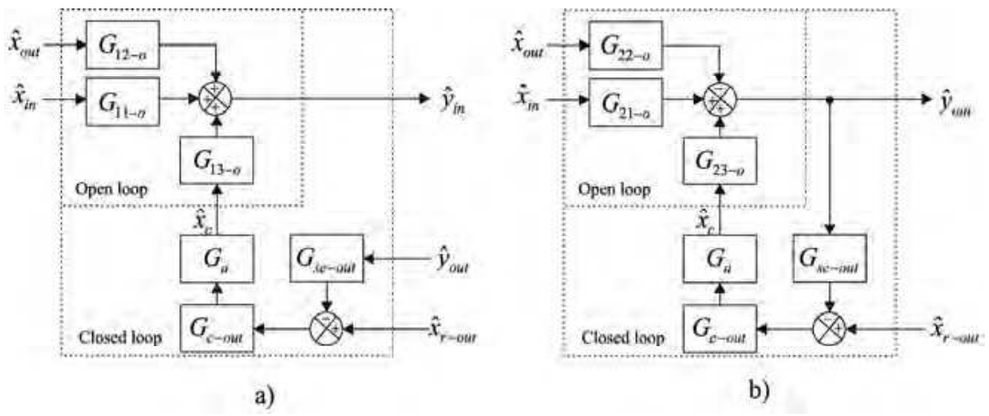

Fig. 13. General closed-loop a) input and b) output control block diagrams under output-side control

$$\begin{bmatrix}\hat{y}_{\text{in}}\\ \hat{y}_{\text{out}}\end{bmatrix}=\begin{bmatrix}\left(\dfrac{G_{11\text{-o}}}{1+L_{\text{out}}}+\dfrac{L_{\text{out}}G_{11\text{-}\infty}}{1+L_{\text{out}}}\right) & \left(\dfrac{G_{12\text{-o}}}{1+L_{\text{out}}}+\dfrac{L_{\text{out}}G_{12\text{-}\infty}}{1+L_{\text{out}}}\right) & \dfrac{G_{13\text{-o}}}{G_{\text{se-out}}G_{23\text{-o}}}\dfrac{L_{\text{out}}}{1+L_{\text{out}}}\\ \dfrac{G_{21\text{-o}}}{1+L_{\text{out}}} & -\dfrac{G_{22\text{-o}}}{1+L_{\text{out}}} & \dfrac{1}{G_{\text{se-out}}}\dfrac{L_{\text{out}}}{1+L_{\text{out}}}\end{bmatrix}\begin{bmatrix}\hat{x}_{\text{in}}\\ \hat{x}_{\text{out}}\\ \hat{x}_{\text{r-out}}\end{bmatrix} \tag{5}$$

$$G_{11\text{-}\infty}=G_{11\text{-o}}-\frac{G_{21\text{-o}}G_{13\text{-o}}}{G_{23\text{-o}}}\qquad G_{12\text{-}\infty}=G_{12\text{-o}}+\frac{G_{21\text{-o}}G_{13\text{-o}}}{G_{23\text{-o}}} \tag{6}$$

The ideal transfer functions defined in (4) and (6) reserves their values despite the state of any feedback and they are usually also specific for a given topology (Suntio, 2009). It may be also obvious that they usually define, especially, the low-frequency behaviour of the corresponding closed-loop transfer functions. The low-frequency value of the ideal transfer function $G_{11-\infty}\approx -\text{Y}_{\text{in}}/\text{X}_{\text{in}}$ (Suntio, 2009), which is usually the origin of the instability problems in the interfacing of a PV generator.

3.1.2 Source and load interactions

The input and output sources are, in practice, non-ideal containing some source impedance, which may significantly affect the dynamic performance of the converter in terms of transient behaviour and stability. The source effect can be computed, in general, based on Fig. 14, where the converter subsystem **C** is connected in cascade with the source subsystem **S** containing either voltage or current source with an internal ohmic non-ideality denoted by S_{22}. The input variables of the system are denoted by ($\hat{x}_{\text{in1}}, \hat{x}_{\text{out2}}, \hat{x}_c$), the output variables by ($\hat{y}_{\text{in1}}, \hat{y}_{\text{out2}}$), and the intermediate variables by ($\hat{x}_{\text{s}}, \hat{y}_{\text{s}}$), respectively. The dynamic representations of the subsystems are given in (7), and the source-affected representation of the converter in (8), respectively, where $G_{11\text{-xo}}$ (9) denote the ohmic characteristics of the input port when the output port is either short circuited (sc) or open circuit (oc) depending on the nature of the ideal load (i.e., the output port is terminated with the inverse of the ideal load impedance). According to (8), the ideal transfer function $G_{11\text{-}\infty}$ (6) determines partly the source effect on the control-to-output transfer function G_{23}, i.e., the output control dynamics.

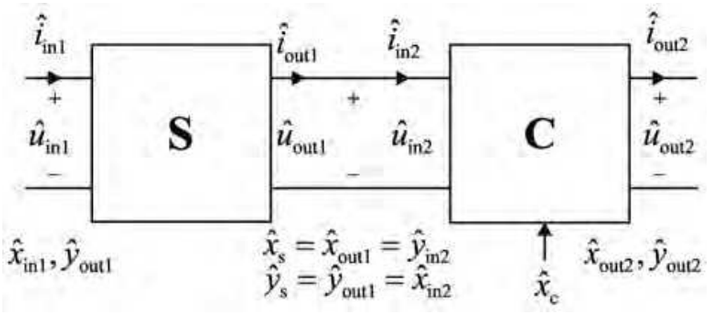

Fig. 14. The cascaded connection of the non-ideal source and the converter

$$\begin{bmatrix} \hat{y}_{\text{in1}} \\ \hat{y}_{\text{s}} \end{bmatrix} = \begin{bmatrix} 0 & 1 \\ 1 & -S_{22} \end{bmatrix} \begin{bmatrix} \hat{x}_{\text{in1}} \\ \hat{x}_{\text{s}} \end{bmatrix} \qquad \begin{bmatrix} \hat{x}_{\text{s}} \\ \hat{y}_{\text{out2}} \end{bmatrix} = \begin{bmatrix} G_{11} & G_{12} & G_{13} \\ G_{21} & -G_{22} & G_{23} \end{bmatrix} \begin{bmatrix} \hat{y}_{\text{s}} \\ \hat{x}_{\text{out2}} \\ \hat{x}_{\text{c}} \end{bmatrix} \tag{7}$$

$$\begin{bmatrix} \hat{y}_{\text{in2}} \\ \hat{y}_{\text{out2}} \end{bmatrix} = \begin{bmatrix} \dfrac{G_{11}}{1+S_{22}G_{11}} & \dfrac{G_{12}}{1+S_{22}G_{11}} & \dfrac{G_{13}}{1+S_{22}G_{11}} \\ \dfrac{G_{21}}{1+S_{22}G_{11}} & -\dfrac{1+S_{22}G_{11\text{-xo}}}{1+S_{22}G_{11}}G_{22} & \dfrac{1+S_{22}G_{11\text{-}\infty}}{1+S_{22}G_{11}}G_{23} \end{bmatrix} \begin{bmatrix} \hat{x}_{\text{in1}} \\ \hat{x}_{\text{out2}} \\ \hat{x}_{\text{c}} \end{bmatrix} \tag{8}$$

$$G_{11\text{-xo}} = G_{11\text{-sco}} = G_{11\text{-oco}} = G_{11} + \frac{G_{12}G_{21}}{G_{22}} \tag{9}$$

The load effect can be computed based on Fig. 15, where the converter subsystem **C** is connected in cascade with the load subsystem **L** containing either a current or voltage sink with the internal ohmic non-ideality denoted by L_{11}. The input, output, and intermediate variables are the same as defined above. The dynamic representations of the subsystems are

given in (10), and the load-affected representation of the converter in (11), respectively, where $G_{22\text{-xi}}$ (12) denote the ohmic characteristics of the output port when the input port is either open circuit (oc) or short circuited (sc) depending on the nature of the ideal source (i.e., the input port is terminated with the inverse of the impedance of the ideal load). According to (11), the ideal transfer function $G_{22\text{-}\infty}$ (4) determines partly the source effect on the control-to-input transfer function G_{13}, i.e., the input control dynamics.

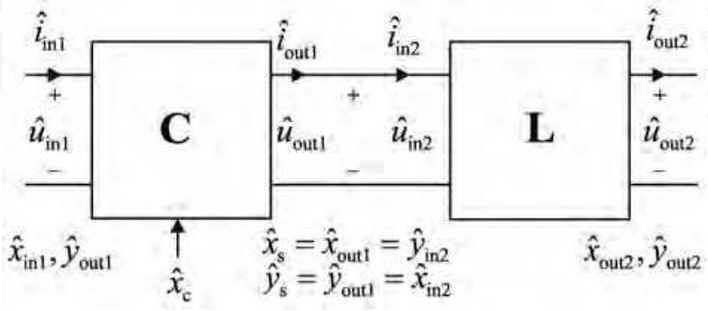

Fig. 15. The cascaded connection of the converter and the non-ideal load

$$\begin{bmatrix} \hat{y}_{in1} \\ \hat{y}_s \end{bmatrix} = \begin{bmatrix} G_{11} & G_{12} & G_{13} \\ G_{21} & -G_{22} & G_{23} \end{bmatrix} \begin{bmatrix} \hat{x}_{in1} \\ \hat{x}_s \\ \hat{x}_c \end{bmatrix} \qquad \begin{bmatrix} \hat{x}_s \\ \hat{y}_{out2} \end{bmatrix} = \begin{bmatrix} L_{11} & 1 \\ 1 & 0 \end{bmatrix} \begin{bmatrix} \hat{y}_s \\ \hat{x}_{out2} \end{bmatrix} \tag{10}$$

$$\begin{bmatrix} \hat{y}_{in1} \\ \hat{y}_{out1} \end{bmatrix} = \begin{bmatrix} \dfrac{1+L_{22}G_{22\text{-xi}}}{1+L_{22}G_{22}} G_{11} & \dfrac{G_{12}}{1+L_{22}G_{22}} & \dfrac{1+L_{22}G_{22\text{-}\infty}}{1+L_{22}G_{22}} G_{13} \\ \dfrac{G_{21}}{1+L_{22}G_{22}} & -\dfrac{G_{22}}{1+L_{22}G_{22}} & \dfrac{G_{23}}{1+L_{22}G_{22}} \end{bmatrix} \begin{bmatrix} \hat{x}_{in1} \\ \hat{x}_{out2} \\ \hat{x}_c \end{bmatrix} \tag{11}$$

$$G_{22\text{-xi}} = G_{22\text{-sci}} = G_{22\text{-oci}} = G_{22} + \frac{G_{12}G_{21}}{G_{11}} \tag{12}$$

3.1.3 General stability assessment

It is well known that the stability of a VF interconnected system consisting of a source and load subsystem can be determined by means of a certain impedance ratio known as minor-loop gain by applying Nyquist stability criterion (Middlebrook, 1976; Zenger, et al., 2006). The impedance-ratio-based method can be generalized to cover all type of interconnected systems with an assumption that the output mode of the source subsystem has to be a dual of the input mode of the load subsystem at the interface under consideration (See Fig. 11).

Fig. 16 shows an arbitrary interconnected system, where the source (**S**) and load (**L**) subsystems are assumed to contain the merged dynamical effects from the downstream and upstream parts of the overall system, respectively. The input, output, and intermediate variables are the same as defined in Section 3.1.2 but the control variable $\hat{x}_c$ is assumed to be zero without loss of generality.

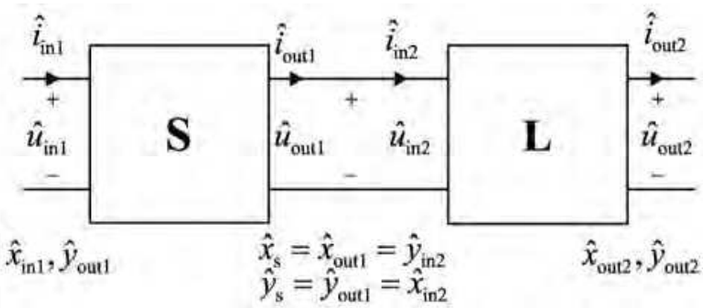

Fig. 16. An interconnected system

The subsystems can be represented by their transfer functions as defined in (13) by utilizing the intermediate variables (See Fig. 16). The stability of the interconnected system can be studied by developing the mappings from the system input variables to the intermediate variables and to the system output variables. These mappings are given in (14) and (15), respectively. If the original subsystems are stable as stand-alone systems then the stability of the interconnected system is dependent on $1/(1+S_{22}L_{11})$ (Zenger, et al., 2006). Stable operation requires that the roots of $(1+S_{22}L_{11})$ have to locate on the left half plane (LHP) of the complex plane (Zenger, et al., 2006), which is ensured when the term $S_{22}L_{11}$ is stable in Nyquist sense. The boundary for the instability is $S_{22}L_{11}=-1$, which means that the impedances forming the term have equal magnitudes and phase shift of 180 degrees. In case of VF interconnected system, $S_{22}L_{11}=Z_{\text{out-S}}/Z_{\text{in-L}}$ (i.e., the minor-loop gain defined by (Middlebrook, 2006)). In case of CF interconnected system, $S_{22}L_{11}=Z_{\text{in-L}}/Z_{\text{out-S}}$ (i.e., the inverse minor-loop gain defined by (Suntio, et al., 2010b)).

$$\begin{bmatrix}\hat{y}_{\text{out1}}\\ \hat{y}_s\end{bmatrix}=\begin{bmatrix}S_{11} & S_{12}\\ S_{21} & -S_{22}\end{bmatrix}\begin{bmatrix}\hat{x}_{\text{in1}}\\ \hat{x}_s\end{bmatrix}\qquad\begin{bmatrix}\hat{x}_s\\ \hat{y}_{\text{out2}}\end{bmatrix}=\begin{bmatrix}L_{11} & L_{12}\\ L_{21} & -L_{22}\end{bmatrix}\begin{bmatrix}\hat{y}_s\\ \hat{x}_{\text{in2}}\end{bmatrix} \tag{13}$$

$$\begin{bmatrix}\hat{x}_s\\ \hat{y}_s\end{bmatrix}=\begin{bmatrix}\dfrac{S_{21}L_{11}}{1+S_{22}L_{11}} & \dfrac{L_{12}}{1+S_{22}L_{11}}\\ \dfrac{S_{21}}{1+S_{22}L_{11}} & -\dfrac{S_{22}L_{12}}{1+S_{22}L_{11}}\end{bmatrix}\begin{bmatrix}\hat{x}_{\text{in1}}\\ \hat{x}_{\text{out2}}\end{bmatrix} \tag{14}$$

$$\begin{bmatrix}\hat{y}_{\text{in1}}\\ \hat{y}_{\text{out2}}\end{bmatrix}=\begin{bmatrix}S_{11}+\dfrac{S_{12}S_{21}L_{11}}{1+S_{22}L_{11}} & \dfrac{S_{12}L_{12}}{1+S_{22}L_{11}}\\ \dfrac{S_{21}L_{21}}{1+S_{22}L_{11}} & -\left(L_{12}+\dfrac{S_{12}S_{22}L_{12}}{1+S_{22}L_{11}}\right)\end{bmatrix}\begin{bmatrix}\hat{x}_{\text{in1}}\\ \hat{x}_{\text{out2}}\end{bmatrix} \tag{15}$$

3.1.4 Theoretical interfacing constraints

As discussed earlier, the constant-current property of the input port of VF converters (See Fig. 11) implies that their operation is limited to the constant-voltage region of the PV generator, because the input current controller would easily saturate due to the violation of Kirchhoff's current law if the operation point is moved to the constant-current region

(Suntio, et al., 2010a). This means also that the real global MPP cannot be traced in the case of shaded PV generator, because the only possible operation region is the constant-voltage region locating at the highest voltages. Similar violation of the Kirchhoff's laws would not take place in the CF converter under input-voltage control (Suntio, et al., 2010b).

According to (5), the low-frequency value of the closed-loop ohmic transfer function G_{11-c} under output-side feedback control (Fig. 13) equals the ideal transfer function $G_{11-\infty}$, which is known to posses the properties of negative resistance (Middlebrook, 1976; Suntio, 2009; Suntio, et al., 2010a&b). According to (Mäki, et al. 2010) the dynamic output impedance of the PV generator is pure resistance at the low frequencies and equals the corresponding static resistance at any of the MPPs (Thongpron, et al., 2006). As a consequence, VF and CF converters become unstable if the operating point is moved to the MPP under output-side feedback control, because both of the minor-loop gains equal -1 at the MPP. According to this, the operation region of the VF converter is limited to the voltages higher than the MPP and the operation region of the CF converter to the voltages lower than the MPP, respectively (Suntio, et al., 2010a&b).

Under input-side feedback control, the closed-loop ohmic transfer function G_{11-c} (See (3)) does not possess properties, which resembles negative resistance. Therefore, the converter stays stable in the minor-loop sense (Suntio, et al., 2010a&b).

The source-affected control-to-output transfer function G_{23}^{S} in (8) has a numerator term $(1+S_{22}G_{11\text{-}\infty})$, which is dependent on the internal impedance of the source and the ideal ohmic behaviour of the input terminal of the converter. According to the discussions above, the numerator term will be zero at the vicinity of the MPP and will also change the phase of the transfer function by 180 deg. This implies instability to take place under output feedback control, when the operating point crosses the MPP. It may be obvious that in case of the cascaded control, where the output-side feedback loop is the inner loop as in the grid-connected PV inverters (See (Blaabjerg, et al., 2006)), the output feedback loop will be unstable and will experience high gain reduction in the vicinity of the MPP. The consequences are not treated here.

4. Current-fed converter implementation

A CF converter can be implemented in three distinct ways such as i) constructing intuitively the converter based on the application of capacitive switched cells (Shmilovitz, 2006), ii) from a VF converter applying duality-transformation methods (Ćuk, 1979), and iii) adding a capacitor at the input terminal of a VF conventional (Leppäaho, et al., 2010). The first method produces a converter with the desired feature defined by the designer. The second method produces a converter having similar static and dynamic properties as the original VF converter has but the input and output variables are interchanged. The third method produces a converter, which has the properties of the dual of the original VF converter, i.e., a VF buck converter transforms into a CF boost converter and vice versa. The converter produced by the third method is not usually recognized to be a CF converter but treated as if it has the properties of the original converter. This is explicitly shown in (Villalva, et al., 2010) and justified by means of the voltage-type characteristics of the PV generator when a capacitor is placed at its output.

4.1.1 Duality transformation

The most convenient method to perform the duality transformation is to place a dot inside every mesh of the electrical circuit, one outside the circuit, and connecting the nodes with the dual of the branch circuit between the nodes (Ćuk, 1979). The duality-transformation process is described by means of an example in Fig. 17: Fig. 17a shows the original VF converter known as superbuck converter (Suntio, 2009). Fig. 17b shows the placement of the nodes inside the meshes and the duals of the branches between the nodes. Fig. 17c shows the resulting CF superbuck converter, which is described more in detail in (Leppäaho & Suntio, 2011). The described method is straightforward and quite easy to apply. The superbuck converter provides continuous input and output voltages and currents, which makes it a desired converter in many applications. The detailed properties of the VF superbuck converter can be found from (Suntio, 2009).

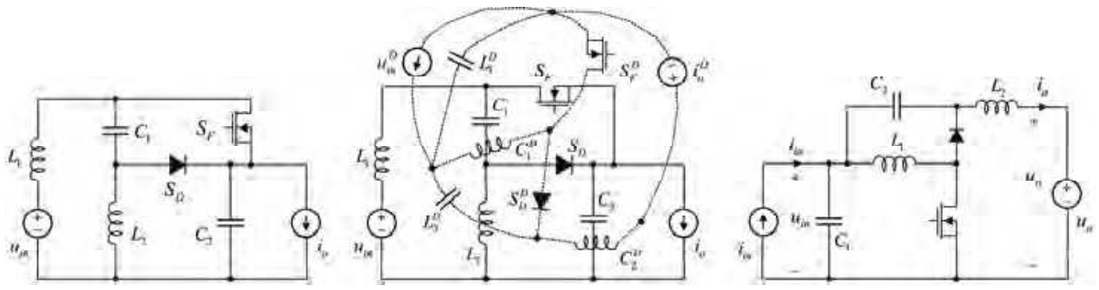

a) b) c)

Fig. 17. Performing the duality transformation: a) VF superbuck converter, b) duality process, and c) CF superbuck converter

4.1.2 Input-capacitor-based transformation

The conventional buck converter in the PV applications is shown in Fig. 18 equipped with an input capacitor. The ideal voltage source at the output terminal short circuits the output capacitor and therefore, it is usually omitted as in (Villalva, et al., 2010). The normal switch control scheme in the conventional buck converter is such that the high-side switch conducts during the on time and the low-side switch during the off time, respectively. The intention is usually to control the input voltage to the MPP of the PV generator. It has been observed that the normal negative feedback control does not work but the polarity of the feedback signal and its reference has to be inverted. This can be easily deduced from Fig. 18: If the input voltage (i.e., the PV voltage) is too low and the conduction time of the high-side switch is increased, the PV voltage would further decrease. If the conduction time of the high-side switch is, however, decreased, the desired effect will be obtained. Similar effect can be obtained by inversing the switch control signals (Leppäaho, et al., 2010) or using a descending PWM ramp signal.

The described controlling scheme of the converter implies that the ideal input-output relation *M(D)=1/(1-D)*, which is a characteristic property of a boost converter. The buck power stage with an input capacitor is, actually, the power stage of a CF boost converter. This fact is not usually recognized but the input capacitor is assumed not to contribute to the dynamic processes inside the converter. Leppäaho, et al., 2010, have definitively shown that the converter contains a right-half-plane (RHP) zero and duty-ratio-dependent resonant behaviour (i.e., second-order dynamics) in its output control dynamics, which are not

present in the original buck converter when its output is terminated with a constant-voltage type load. The PV generator removes the RHP zero and the resonant behaviour when the operating point moves to the constant-voltage region. This is understandable, because the low resistance value of the output impedance of the PV generator effectively removes the effect of the input capacitor.

Similarly, the conventional boost power stage with an input capacitor will constitute a converter having properties of a CF buck converter with an input LC filter (See e.g. (Xiao, et al., 2007a&b)).

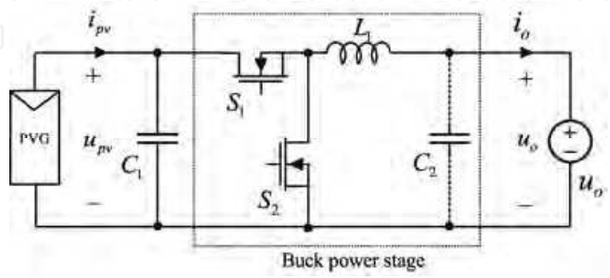

Fig. 18. Buck-power-stage-based converter

5. Experimental evidence

The experimental converters are shown in Fig. 19 and supplied by Raloss SR30-36 panel discussed earlier in Section 2. The more detailed information on the converters can be found from (Huusari, et al., 2010; Leppäaho, et al., 2010). The same frequency response analyzer as in Section 2 is used to extract the frequency responses shown below.

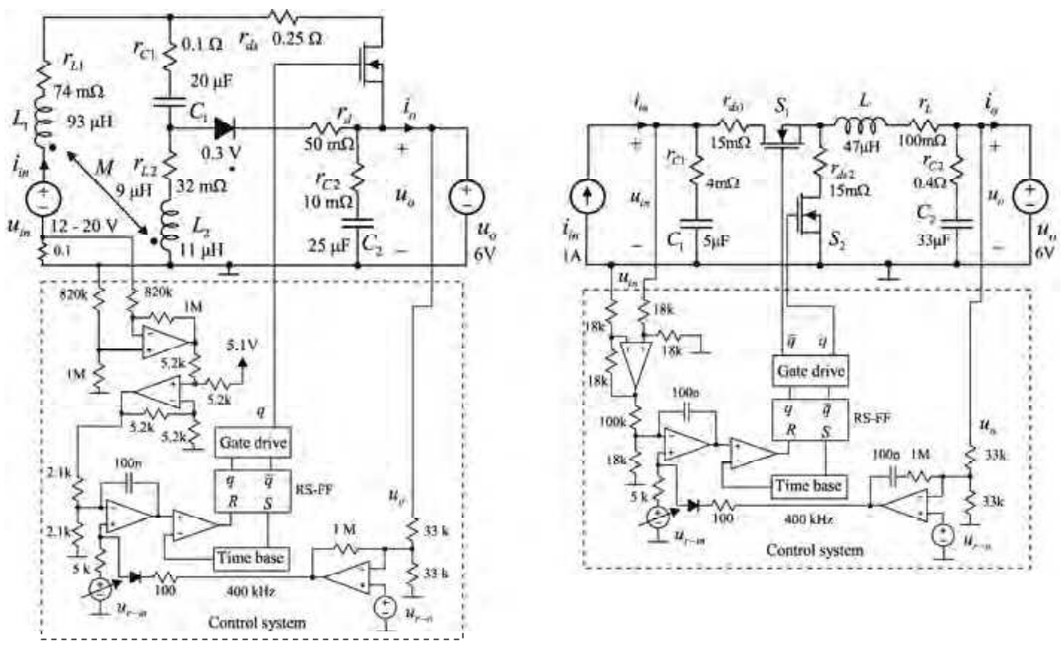

a) b)

Fig. 19. The experimental converters: a) VF superbuck converter, and b) CF boost converter

Fig. 20a shows the measured input impedances and the output impedances of the PV generator covering the same operating points as Fig. 20b, where the time-domain behaviour of the VF superbuck converter (Fig. 19a) is shown when its input-current reference is swept from 0.25 A to 0.92 A and back, and where the highest-current operating point is slightly in the constant-current region beyond the MPP.

According to Fig.20a, it is clear that the converter is stable in the minor-loop-gain sense (Middlebrook, 1979). Fig. 20b shows that the input voltage (u_{sg}) collapses and the converter ceases to operate when the Kirchhoff's current law (KCL) is violated but recovers when the reference is sufficiently changed back to the constant-voltage region. The behaviour of the VF converter is as discussed in Subsection 3.1.4 when the violation of the KCL takes place.

Fig. 21a shows the measured input impedances of the CF converter (Fig. 19b) and the output impedances of the PV generator when the output-voltage-limiting control is active and the operating point approaches the MPP from the constant-current region. The corresponding minor-loop gain indicates instability to take place at the MPP (Suntio, et al., 2010b). Fig. 21b shows the time-domain behaviour of the converter when the operating point is placed in the constant-voltage region (17 V) and the output-voltage-limiting control is activated. The instability moves the operating point quickly to the constant-current region, where the operation is stable. This phenomenon is one of the beneficial features of the CF converters but it shall be noticed that the MPP-tracking device shall not try to move the operating point anymore back to the MPP because of the instability to take place. Fig. 21a shows also that the low-frequency input impedance of the CF converter under output-side control is a negative resistance as discussed in Subsection 3.1.4. Under input-voltage control, the CF converters are capable to operate within the whole range of the PV operating points valid for the certain converter topology.

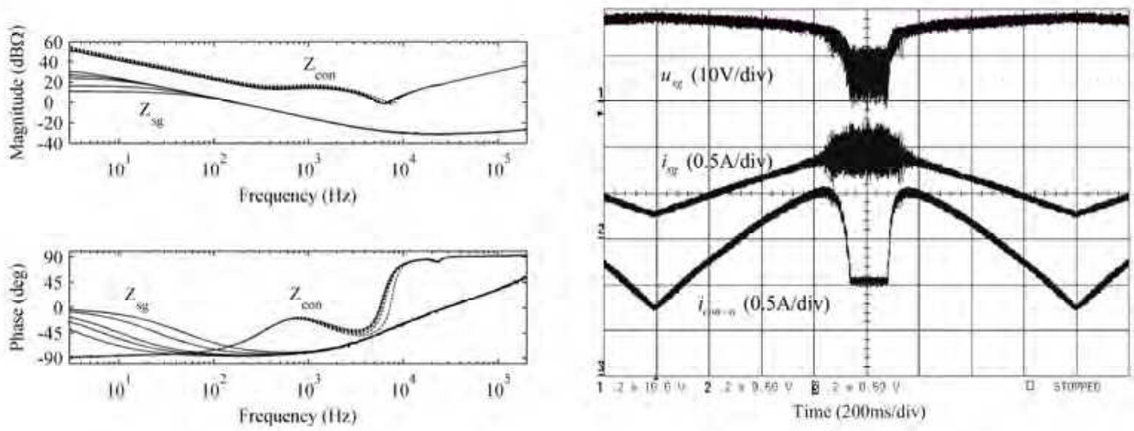

a) b)

Fig. 20. a) The input impedances of the VF converter and the output impedances of the PV generator, and b) The time-domain behaviour of the VF converter when its input-current reference is swept from 0.25 A to 0.92 A and back starting from the constant-voltage region and entering slightly into the constant-current region beyond the MPP

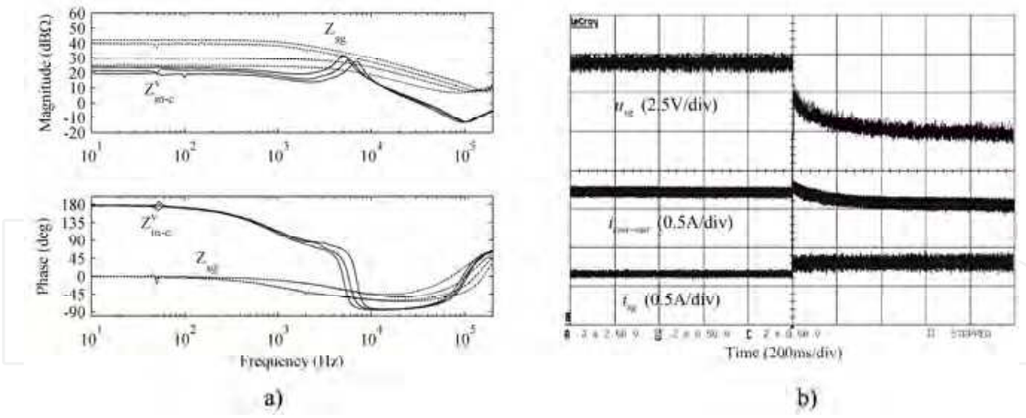

Fig. 21. a) The input impedances of the CF converter under output-voltage-limiting control and the output impedances of the PV generator when the operating point moves toward the MPP, and b) The time-domain behaviour of the CF converter when its operating point is placed in the constant-voltage region at 17 V and the output-voltage-limiting controller is activated

Fig. 22 shows the behaviour of the measured control-to-output-current transfer function of the CF boost converter (Fig. 19b) when the operating point crosses the MPP. It shows that the phase of the transfer function changes by 180 degrees implying instability to take place under output-side feedback control as discussed in Subsection 3.1.4 and shown to take place in Fig. 22b. The transfer function (14 V) shows also the existence of RHP zero and second-order nature of the converter, which are removed in the constant-voltage region (16 V).

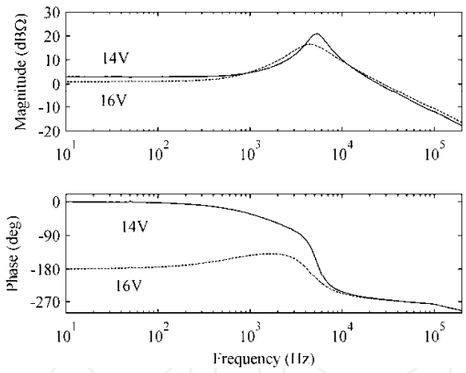

Fig. 22. The behaviour of the control-to-output-current transfer function of the CF boost converter when the operating point is moved from the constant-current region (14 V) to the constant-voltage region (16 V)

6. Summary

The interfacing constraints of PV generator as well as the real nature of the interfacing converters were introduced. It was defined and experimentally proved that the VF converter can operate only in the constant-voltage region of the PV generator. This means also that the MPP, up to which it can operate, is the highest-voltage MPP. Therefore, its MPP-tracking efficiency is rather poor especially in case of the shaded conditions in the PV generator. The

CF converters do not suffer from similar constraints when the input voltage is controlled but become unstable at the MPP or the voltages higher than the MPP under output voltage or current feedback control.

It was also explicitly stated that the power stage of the converter does not necessarily determine the true nature of the converter but the input and output sources and the feedback signals used. These facts are not well understood and therefore, the analyses of the converter in PV applications are most often deficient or even erroneous.

The resistive nature of the output impedance of the PV generator has tremendous effect on the dynamics of the converter connected directly to it. The most significant changes are taken place in the output control dynamics such as the change of phase by 180 degrees when crossing the MPP, the reduction of the gain of the control-to-output transfer function significantly at the MPP, the appearing/disappearing of right-half-plane zeros, etc. All these changes may have fundamental and catastrophic effect on the operation of the PV converters and inverters.

7. Acknowledgment

The contributions of Professor *Seppo Valkealahti*, and the PhD students *Juha Huusari*, *Jari Leppäaho*, *Tuomas Messo*, *Anssi Mäki*, *Lari Nousiainen*, *Joonas Puukko,* and *Diego Torres Lobera* are greatly appreciated and vital to the content of this chapter.

8. References

Anantha Krishna, H.; Misra, N. K. & Suresh, M. S. Solar Cell as a Capacitive Temperature Sensor. *IEEE Transactions on Aerospace and Electronic Systems*, Vol.47, No.2, (April 2011), pp. 782-789, ISSN 0018-9251.

Blaabjerg, F.; Teodorescu, R; Liserre, M., & Timbus, A. Overview of Control and Grid Synchronization for Distributed Generation Systems. *IEEE Transactions on Industrial Electronics*, Vol.53, No.5, (October 2006), pp. 1398-1409, ISSN 0278-0046.

Bose, B. K. Global Warming: Energy, Environmental Pollution, and the Impact of Power Electronics. *IEEE Industrial Electronics Magazine*, Vol.4, No.1, (March 2010), pp. 6-17, ISSN 1932-4529.

Bull, S. R. Renewable Energy Today and Tomorrow. *Proceedings of The IEEE*, Vol.89, No.8, (August 2001), pp. 1216-1226, ISSN 0018-9219.

Capel, A.; Marpinard, J. C.; Jalade, J. & Valentin, M. Current Fed and Voltage Fed Switching DC/DC Converters – Steady State and Dynamic Models, Their Applications in Space Technology. *International Telecommunications Energy Conference*, pp. 421-430, ISBN 83CH1855-6, Tokyo, Japan, 18-21 October, 1983.

Dehbonei, H.; Lee, S. R. & Nehrir, H. Direct Energy Transfer for High Efficiency Photovoltaic Energy Systems. Part I: Concepts and Hypothesis. *IEEE Transactions on Aerospace and Electronic Systems*, Vol.45, No. 1, (January 2009a), pp. 31-45, ISSN 0018-9251.

Dehbonei, H.; Lee, S. R. & Nehrir, H. Direct Energy Transfer for High Efficiency Photovoltaic Energy Systems. Part II: Experimental Evaluation. *IEEE Transactions on Aerospace and Electronic Systems*, Vol.45, No. 1, (January 2009b), pp. 46-57, ISSN 0018-9251.

Ćuk, S. General Topological Properties of Switching Structures. *IEEE Power Electronic Specialists Conference*, pp. 109-130, ISBN 79CH1461-3, San Diego, CA, USA, 18-22 June, 1979.

Esram, T. & Chapman, P. L. Comparison of Photovoltaic Array Maximum Power Point Tracking Techniques. *IEEE Transactions on Energy Conversion*, Vol. 22, No.2, (June 2007), pp. 439-449, ISSN 0885-8969 .

Femia, N.; Lisi, G.; Petrone, G. & Vitelli, M. Distributed Maximum Power Point Tracking of Photovoltaic Arrays: Novel Approach and System Analysis. *IEEE Transactions on Industrial Electronics*, Vol.55, No.7, (July 2008), pp. 2610-2621, ISSN 0278-0046.

Huusari, J.; Leppäaho, J. & Suntio T. Dynamic Properties of PCM-Controlled Superbuck Converter – Discrete vs. Coupled Inductor Implementation. *European Power Electronics and Drives Journal*, Vol.20, No.2, (June 2010), pp. 31-40, ISSN 0939-8368.

Jain, S. & Agarwal, V. Comparison of Performance of Maximum Power Point Tracking Schemes Applied to Single-Stage Grid Connected Photovoltaic Systems. *IET Electrical Power Applications*, Vol. 1, No.5, (September 2007), pp. 753-762, ISSN 1751-8660.

Kumar, R. A.; Suresh, M. S. & Nagaraju, J. Effect of Solar Array Capacitance on the Performance of Switching Shunt Regulator. *IEEE Transactions on Power Electronics*, Vol.21, No.2, (March 2006), pp. 543-548, ISSN 0885-8993.

Leppäaho, J.; Nousiainen, L.; Puukko, J.; Huusari, J. & Suntio, T. Implementing Current-Fed Converters by Adding an Input Capacitor at the Input of Voltage-Fed Converter for Interfacing Solar Generator. *International Power Electronics and Motion Control Conference*, pp. 81-88, ISBN 978-1-4244-7855-2, Ohrid, Republic of Macedonia, 6-8 September, 2010.

Leppäaho, J. & Suntio, T. Dynamic Characterization of Current-Fed Superbuck Converter. *IEEE Transactions on Power Electronics*, Vol.26, No.1, (January 2011), pp. 200-209, ISSN 0885-8993.

Lyi, S. & Dougal, R. A. Dynamic Multiphysics Model for Solar Array. *IEEE Transactions on Energy Conversion*, Vol. 17, No.2, (June 2002), pp. 285-294, ISSN 0885-8969.

McLaughlin, J. C. & Kaiser, K. L. Deglorifying the Maximum Power Transfer Theorem and Factors in Impedance Selection. *IEEE Transactions on Education*, Vol.50, No.3, (August 2007), pp. 251-255.

Menti, A.; Zacharias, T. & Milias-Argitis, J. Harmonic Distortion Assessment for Single-Phase Grid-Connected Photovoltaic Systems. *Renewable Energy*, Vol.36, No.1, (January 2011), pp. 360-368, ISSN 0038-092X

Middlebrook, R. D. Input Filter Considerations in Design and Applications of Switching Regulators. *IEEE Industry Application Society Annual Conference*, pp. 366-382, ISBN 76CH1122-1-IA, Chigago, IL, USA, 1976.

Mäki, A.; Valkealahti, S. & Suntio, T. Dynamic Terminal Characteristics of a Solar Generator. *International Power Electronics and Motion Control Conference*, pp. 76-80, ISBN 978-1-4244-7855-2, Ohrid, Republic of Macedonia, 6-8 September, 2010.

Park, J.-H.; Ahn, J.-Y.; Cho, B.-H., & Yu, G.-J. Dual-Module-Based Maximum Power Point Tracking Control of Photovoltaic Systems. *IEEE Transactions on Industrial Electronics*, Vol.53, No.4, (August 2006), pp. 1036-1047, ISSN 0278-0046.

Petrone, G.; Spagnuolo, G.; Teodorescu, R.; Veerachary, M. & Vitelli, M. Reliability Issues in Photovoltaic Power Processing Systems. *IEEE Transactions on Industrial Electronics*, Vol.55, No.7, (July 2008), pp. 2569-2580, ISSN 0278-0046.

Rahman, S. Green Power: What Is It and Where Can We Find It? *IEEE Power & Energy Magazine*, Vol.1, No.1, (January-February 2003), pp. 30-37, ISSN 1540-7977.

Salas, V., Olias, E.; Barrado, A. & Lazaro A. Review of the Maximum Power Point Tracking Algorithms for Stand-Alone Photovoltaic Systems. *Solar Energy Materials & Solar Cells*, Vol.90, No.12, (July 2006), pp. 1555-1578, ISSN 0927-0248.

Sanchis, P.; Lopez, J., Ursua, A.; Gubia, E. & Maroyo, L. On Testing, Characterization, and Evaluation of PV Inverters and Dynamic MPPT Performance under Real Varying Operating Conditions. *Progress in Photovoltaics: Research and Applications*, Vol.15, No.6, (September 2007), pp. 541-556, ISSN 1099-159X.

Shmilovitz, D. & Singer, S. A Switched Mode Converter Suitable for Superconductive Magnetic Energy Storage (SMES) Systems. *IEEE Applied Power Electronics Conference*, pp. 630-634, ISBN 7803-7404, Dallas, TX, USA, 10-14 March, 2002.

Shmilovitz, D. Gyrator Realization Based on a Capacitive Switched Cell. *IEEE Transactions on Circuits and Systems I: Regular Papers*, Vol.53, No.12, (December 2006), pp. 1418-1422, ISSN 1549-8328.

Siri, K. Study of System Instability in Solar-Array-Based Power Systems. *IEEE Transactions on Aerospace and Electronic Systems*, Vol.36, No.3, (July 2000), pp. 957-964, ISSN 0018-9251.

Suntio, T. (2009). Dynamic *Profile of Switched-Mode Converter: Modeling, Analysis and Control*. Wiley-VCH, ISBN 978-3-527-40708-8, Weinheim, Germany

Suntio, T.; Huusari, J. & Leppäaho, J. Issues on Solar-Generator Interfacing with Voltage-Fed MPP-Tracking Converters. *European Power Electronics and Drives Journal*, Vol.20, No.3, (September 2010a), pp. 40-47, ISSN 0939-8368.

Suntio, T.; Leppäaho, J.; Huusari, J. & Nousiainen, L. Issues on Solar-Generator Interfacing with Current-Fed MPP-Tracking Converters. *IEEE Transactions on Power Electronics*, Vol.25, No.9, (September 2010b), pp. 2409-2418, ISSN 0885-8993.

Thongpron, J.; Kirtikara, K. & Jivicate, C. A Method for Determination of Dynamic Resistance of Photovoltaic Modules under Illumination. *Solar Energy Materials & Solar Cells*, Vol.90, No.18/19, (November 2006), pp. 3078-3084, ISSN 0927-0248.

Tse, C. K. (1998). Linear Circuit Analysis. Addison-Wesley, ISBN 0-201-34296-0, Harlow, England.

Villalva, M. G.; Gazoli, J. R. & Filho, E. R. Comprehensive Approach to Modeling and Simulating Photovoltaic Arrays. *IEEE Transaction on Power Electronics*, Vol. 24, No.5, (May 2009), pp. 1198-1208, ISSN 0885-8993.

Villalva, M.; de Siqueira, T. G., and Ruppert, E. Voltage Regulation of Photovoltaic Arrays: Small-Signal Analysis and Control Design. *IET Power Electronics*, Vol.3, No.6, (November 2010), pp. 869-880, ISSN 1755-4535.

Wang, Y.-J. & Hsu, P.-C. Modelling of Solar Cells and Modules Using Piecewise Linear Parallel Branches. *IET Renewable Power Generation*, Vol.5, No.3, (May 2011), pp. 215-222, ISSN 1752-1416.

Xiao, W.; Dunford, W. G.; Palmer, P. R. & Capel, A. Regulation of Photovoltaic Voltage. *IEEE Transaction on Industrial Electronics*, Vol.54, No.3, (June 2007a), pp. 1365-1374, ISSN 0278-0046.

Xiao, W.; Ozog, N. & Dunford, W. G. Topology Study of Photovoltaic Interface for Maximum Power Tracking. *IEEE Transactions on Industrial Electronics*, Vol.54, No.3, (June 2007b), pp. 1696-1704, ISSN 0278-0046.

Zenger, K.; Altowati, A. & Suntio, T. Dynamic Properties of Interconnected Power Systems – A System Theoretic Approach. *IEEE International Conference on Industrial Electronics and Applications*, pp. 835-840, ISBN 7803-9514, Singapore, 24-26 May, 2006.

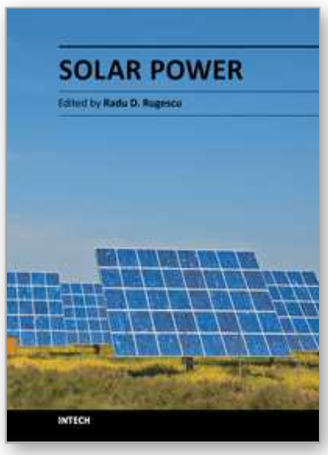

Solar Power

Edited by Prof. Radu Rugescu

ISBN 978-953-51-0014-0
Hard cover, 378 pages
Publisher InTech
Published online 15, February, 2012
Published in print edition February, 2012

A wide variety of detail regarding genuine and proprietary research from distinguished authors is presented, ranging from new means of evaluation of the local solar irradiance to the manufacturing technology of photovoltaic cells. Also included is the topic of biotechnology based on solar energy and electricity generation onboard space vehicles in an optimised manner with possible transfer to the Earth. The graphical material supports the presentation, transforming the reading into a pleasant and instructive labor for any interested specialist or student.

How to reference

In order to correctly reference this scholarly work, feel free to copy and paste the following:

Teuvo Suntio (2012). Issues on Interfacing Problematics in PV Generator and MPP-Tracking Converters, Solar Power, Prof. Radu Rugescu (Ed.), ISBN: 978-953-51-0014-0, InTech, Available from: http://www.intechopen.com/books/solar-power/issues-on-interfacing-problematics-in-pv-generator-and-mpp-tracking-converters

INTECH
open science | open minds

InTech Europe
University Campus STeP Ri
Slavka Krautzeka 83/A
51000 Rijeka, Croatia
Phone: +385 (51) 770 447
Fax: +385 (51) 686 166
www.intechopen.com

InTech China
Unit 405, Office Block, Hotel Equatorial Shanghai
No.65, Yan An Road (West), Shanghai, 200040, China
中国上海市延安西路65号上海国际贵都大饭店办公楼405单元
Phone: +86-21-62489820
Fax: +86-21-62489821

IntechOpen